Integrated Scramjet Nozzle/Afterbody Performance Analysis

Jonas A. Sadunas*
Rockwell International, Downey, Calif.

A two-dimensional flowfield computer program developed for preliminary performance analysis of integrated scramjets is presented. Scramjet flowfields are computed by means of the shock-capture technique, with real gas thermodynamic properties for frozen and equilibrium compositions. The program computes internal and external flowfields with multiple shock interactions. Interaction of the exhaust (underexpanded or overexpanded) with the external stream and vehicle afterbody also is considered. Forces and moments are computed due to stream thrust and external surface pressure distributions. Typical program results for parametric nozzle/afterbody design and off-nominal performance analysis are presented.

I. Introduction

In recent years, increased attention has been given to the application of supersonic combustion ramjets (scramjets) to airbreathing launch vehicles, advanced civil aviation, and hypersonic research aircraft. One of the scramjet technology areas requiring particular attention is the interaction of the airbreathing propulsion system with the vehicle aerodynamics and the resulting effects on the overall vehicle performance. Particularly significant and as yet not well defined is the interaction of the vehicle afterbody and the exhaust of the integrated scramjet.[1-4] The integrated scramjet propulsion system utilizes the vehicle afterbody as an extension of the nozzle, producing increased effective exhaust velocities and thrust at the expense of incurred trim penalties.

Therefore, a requirement exists for the means to define accurately scramjet nozzle/afterbody exhaust flowfields. A critical review of this problem indicated that detailed analysis should include consideration of real gas three-dimensional flowfields with chemical-kinetic effects, multiple shocks, heat transfer, boundary layer growth, and interaction with the inviscid flow. In view of the complexity of the problem, simplified practical methods of analysis must be developed which retain the most essential features of the flow phenomena, fulfill preliminary design requirements, and produce realistic results.

At the present time, the computer programs of Refs. 5 and 6 appear to be the only published programs specifically developed to meet this requirement. These programs consider inviscid and adiabatic quasi-three-dimensional flowfields with real gas equilibrium hydrogen-air chemistry. These programs are based on the reference plane technique, with a table lookup thermodynamic properties routine.

This paper represents a simpler scramjet flowfield analysis computer program suitable for preliminary design analyses. Since the majority of the current scramjet configurations are of the modular quasi-two-dimensional type, it is felt that for preliminary design purposes the flowfield can be described sufficiently well by means of a two-dimensional program. The two-dimensional scramjet flowfield program[7] considers inviscid and adiabatic supersonic flow in ducts and coflowing dissimilar streams with real or ideal gas properties. The methodology used in this program is the shock capture technique (SCT) described in Refs. 8 and 9. Thermodynamic properties are evaluated by means of a special-purpose subprogram that computes either frozen or chemical equilibrium properties. In addition, the subprogram has a provision for freezing the gas composition during computation such that chemical-kinetic effects could be included at a later date.

Types of flows which may be analyzed by means of this program include flow in symmetric and asymmetric expansions with one free boundary and one specified boundary, e.g., scramjet nozzle exhaust flow over the vehicle afterbody. In the case of the free expansions, the nozzle flow may be under- or overexpanded, and the composition of the external flow could be the same or different from that of the nozzle flow. Program capability is illustrated by presenting results of typical scramjet flowfields and nozzle/afterbody design analyses computed by means of this program.

Presented as Paper 75-1297 at the AIAA/SAE 11th Propulsion Conference, Anaheim, Calif., Sept. 29-Oct. 1, 1975; submitted Oct. 1, 1975; revision received Feb. 13, 1976.

Index categories: Airbreathing Propulsion, Hypersonic; Aircraft Powerplant Design and Installation.

*Member of the Technical Staff, Space Division. Member AIAA.

II. Methodology

Flowfield Equations

The gasdynamic equations for steady two-dimensional flow of a perfect gas can be written in the orthogonal coordinates system[8] as

$$(\partial \bar{E}/\partial x) + (\partial \bar{F}/\partial y) = 0 \tag{1}$$

where $\bar{E}$ and $\bar{F}$ are defined by the three component vectors

$$\bar{E} = \begin{vmatrix} \rho v \\ \rho uv \\ p+\rho v^2 \end{vmatrix}, \quad \bar{F} = \begin{vmatrix} \rho u \\ p+\rho u^2 \\ \rho uv \end{vmatrix} \tag{2}$$

which represent continuity, x momentum, and y momentum, respectively.

Introducing the nonorthogonal coordinate transformation shown in Fig. 1

$$\eta = (y-y_2)/w, \; w = y_n - y_2, \; \zeta = x \tag{3}$$

such that the distance from the lower wall is normalized by the local distance between the lower and upper prescribed flow boundaries.

Then it can be shown that

$$\partial/\partial x = (\partial/\partial \zeta) - (\mu/w)(\partial/\partial \eta) \tag{4a}$$

$$\partial/\partial y = (1/w)(\partial/\partial \eta) \tag{4b}$$

$$\mu = (1-\eta)y_2' + \eta y_n' \tag{4c}$$

and applying this transformation to Eq. (1) yields

$$\frac{\partial \bar{E}}{\partial \zeta} - \frac{\mu}{w}\frac{\partial \bar{E}}{\partial \eta} + \frac{1}{w}\frac{\partial \bar{F}}{\partial \eta} = 0 \tag{5}$$

from which it follows that

$$E=w\bar{E},\ F=\bar{F}-\mu\bar{E} \tag{6}$$

Therefore, the final form of the conservation equation is

$$E=w\begin{vmatrix}\rho u\\ p+\rho u^2\\ \rho uv\end{vmatrix} \tag{7a}$$

$$F=\begin{vmatrix}\rho(v-\mu u)\\ \rho u(v-\mu u)-\mu p\\ \rho v(v-\mu u)+p\end{vmatrix} \tag{7b}$$

$$(\partial E_i/\partial\zeta)+(\partial F_i/\partial\eta)=0,\ i=1,2,3 \tag{8}$$

The solution is obtained by numerical integration of Eq. (8) in the ζ direction. At each step of the integration, it is necessary to evaluate the F conservation variables from the corresponding E variables. This is done by the simultaneous solution of the following four equations

$$E_1=(\rho u)w \tag{9a}$$

$$E_2=(p+\rho u^2)w \tag{9b}$$

$$E_3=(\rho uv)w \tag{9c}$$

$$(u^2+v^2)/2=H_o-\Gamma(p/\rho) \tag{9d}$$

where

$$\Gamma=\gamma_e/(\gamma_e-1)$$

From the preceding equations, we have

$$v=E_3/E_1 \tag{10a}$$

$$u=[B+(B^2-4AC)^{1/2}]/2A \tag{10b}$$

$$p=(E_2/w)-\rho u^2 \tag{10c}$$

where

$$A=\Gamma-\tfrac{1}{2}$$

$$B=\Gamma E_2/E_1$$

$$C=H_o-(v^2/2)$$

and where for the real gas case γ_e is the "effective" ratio of specific heats, and from Eq. (7) it is seen that

$$F_1=[(E_3/u)-\mu E_1]/w \tag{11a}$$

$$F_2=(E_3-\mu E_2)/w \tag{11b}$$

$$F_3=F_1v+p \tag{11c}$$

Finite-Difference Procedure

The partial differential equation (8) representing continuity, x momentum, and y momentum is solved by means of the two-step MacCormack predictor-corrector method described in Ref. 9. The solution proceeds in the ζ direction from a constant ζ plane where the flow properties are known. The first step of the computation (the predictor step) estimates the preliminary values of the E's at the $(k+1)$ plane using the backward differences along the k surface; thus, with reference to Fig. 1

$$\tilde{E}_j^{k+1}=F_j^k-(\Delta x/\Delta\eta)(F_{j+1}^k-F_j^k) \tag{12}$$

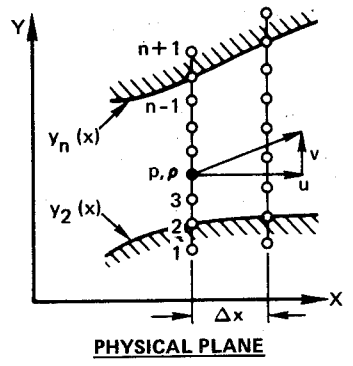

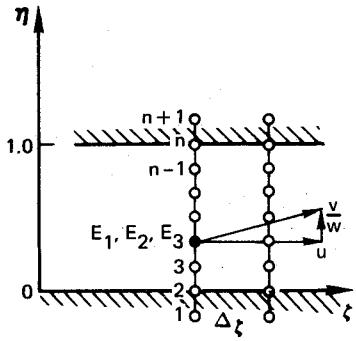

Fig. 1 Coordinate system.

The gasdynamic variables are evaluated next by means of Eq. (1) from the three E values. The corresponding F values in the $(k+1)$ plane then are computed from Eqs. (11). The final values of the E's at the $(k+1)$ surface are obtained from the corrector step, i.e., by averaging the F derivatives in the k and $(k+1)$ planes; thus

$$E_j^{k+1}=\tfrac{1}{2}[E_j^k+\tilde{E}_j^{k+1}-(\Delta x/\Delta\eta)(F_j^{k+1}-\tilde{F}_{j-1}^{k+1})] \tag{13}$$

The computation is completed by evaluating the corresponding gasdynamic properties and the F's by means of Eqs. (10) and (11).

Step Size

In order to minimize computation time, it is desirable to choose the maximum possible step size compatible with stability criteria. According to Refs. 8 and 9, the maximum step size is given by

$$\Delta X\le(w\Delta\eta)\frac{u^2-c^2}{|uv|+c(u^2+v^2-c^2)^{1/2}} \tag{14}$$

which is recognized to be the slope of the characteristics in the x, y plane.

Boundary Conditions

At the solid boundaries, the surface tangency condition must be satisfied. The method employed in this program is due to Abbett and is described in Ref. 8. The procedure consists of 1) computing approximate values of the flow variables using the E's obtained by means of Eq. (12), 2) correcting these quantities using simple compression or expansion waves to satisfy the tangency condition exactly, 3) computing density next using the condition of constant entropy from the previous step, and 4) completing the solution by computing the resultant flow velocity at the wall from the energy equation.

In the case of the free boundary, e.g., the interaction of the expanding jet with the freestream, the solid boundary is replaced by the slip plane. The location of the slip plane is determined iteratively by simultaneous computation of the flowfields on both sides of the slip plane. The location of the slip plane is adjusted with each computation cycle until the pressures are equal on both sides.

Forces and Moments

The forces and moments corresponding to the pressure distribution acting on the upper flow boundary and the stream thrust at prescribed x station (e.g., scramjet inlet or nozzle exit plane) are computed by the program. Referring to Fig. 2, the forces and pitching moment due to the pressure acting on the vehicle surface between x_1 and x_2 are given by

$$F_x = -\int_{x1}^{x2} (p - p_\infty) \frac{dy}{dx} dx \tag{15a}$$

$$F_y = \int_{x1}^{x2} (p - p_\infty) dx \tag{15b}$$

$$M = \int_{x1}^{x2} \left[(p - p_\infty) y \frac{dy}{dx} + (p - p_\infty) x \right] dx \tag{15c}$$

and, at the constant x_2 and x_3 planes, the corresponding forces and moment due to stream thrust are

$$F_x = \int_{yi}^{yn} [(p - p_\infty) + \rho u^2] dy \tag{16a}$$

$$F_y = \int_{yi}^{yn} (\rho u v) dy \tag{16b}$$

$$M = \int_{yi}^{yn} [(p - p_\infty + \rho u^2) y - (\rho u v) x] dy \tag{16c}$$

where y_i is the lower integration y limit, and y_n is the y coordinate of the upper flow boundary.

Thermodynamic Properties

A special-purpose hydrogen-air thermodynamic properties subprogram is incorporated in the scramjet flowfield program. The thermodynamic properties subprogram has the following characteristics: 1) computes P, T, H, S, and ρ from any one pair of given state properties and the equivalence ratio, 2) evaluates frozen or chemical-equilibrium properties, and 3) includes a provision for freezing the composition at any specified state to approximate chemical-kinetic behavior of the gas (to be included at a later date).

The temperature and pressure range for which the program is valid is limited to conditions where the concentrations of species other than the eight considered in the chemical model are less than 10^{-5}. For the stoichiometric mixture, the limiting approximate values of pressure and temperature have been determined to be

$$T = 148.15 \ln P + 3173.0$$

where T is in degrees Kelvin and P in atmospheres. For lean or rich mixtures, these limits may be extended somewhat.

The hydrogen-air thermodynamic properties program is modeled after an undocumented H_2/O_2 real gas subprogram previously developed by E.P. French at Rockwell International's Space Division. The method of equilibrium constants is used to determine the gas composition, with the thermodynamic properties determined from the thermodynamic coefficient data of Ref. 10.

The chemical model consists of the following eight species: N_2, H_2O, H_2, O_2, OH, H, O, and NO. In the temperature-pressure range considered, other species may be present, e.g., N, HO_2, NH_2, NH_3, NO_3; however, their concentrations are less than 10^{-5}. The composition of the mixture at high temperatures is determined by the following five reactions

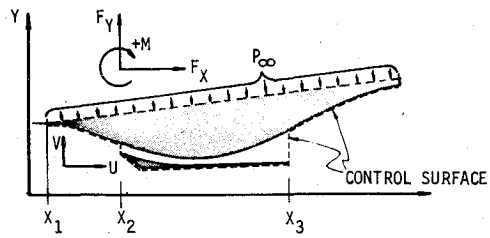

Fig. 2 Force and moment computation coordinate system.

$$\tfrac{1}{2}O_2 + H_2 = H_2O \tag{17a}$$

$$\tfrac{1}{2}H_2 + OH = H_2O \tag{17b}$$

$$2H = H_2 \tag{17c}$$

$$2O = O_2 \tag{17d}$$

$$\tfrac{1}{2}N_2 + \tfrac{1}{2}O_2 = NO \tag{17e}$$

Each reaction is characterized by an equilibrium constant that is a function of temperature and pressure only. In addition, we have the following three atom balance equations

$$2X^\circ_{N_2} = 2X_{N_2} + X_{NO} \tag{18a}$$

$$2X^\circ_{H_2} + 2X^\circ_{H_2O} = 2X_{H_2} + 2X_{H_2O} + X_{OH} + X_H \tag{18b}$$

$$X^\circ_{H_2O} + 2X^\circ_{O_2} = X_{H_2O} + 2X_{O_2} + X_{OH} + X_O + X_{NO} \tag{18c}$$

where $X\tfrac{1}{2}$ is the moles of N_2 per mole of undissociated mixture, and $X^\circ_{N_2}$ is the mole fraction of N_2 in the original undissociated mixture, etc. Thus, for a given mixture pressure and temperature, we have five equations for reactions (17) (relating the mixture composition and the equilibrium constants), which, together with the three atom balance equations (18), are solved iteratively to yield the concentrations of the eight species. Having determined the gas composition, the mixture thermodynamic properties are computed from the thermodynamic coefficient data of Ref. 10.

III. Results

Thermodynamic Properties

A comparison of the thermodynamic properties and composition of a stoichiometric mixture computed by means of this program and those computed by means of the general-purpose program[10] is presented in Fig. 3 and Table 1. The pressure and temperature chosen for this comparison result in a highly dissociated mixture; nevertheless, very good agreement is obtained between the results of the two programs. The slight discrepancies in the composition are due primarily to the simplified chemical model; however, the thermodynamic properties are practically identical. The computation times for the present program were found to be 10 to 15 times faster than for the general-purpose program.

Flowfields

A series of computer program runs was made in connection with the hypersonic research aircraft studies of Ref. 11 to analyze the flow properties of the scramjet configuration shown in Fig. 4. The flight condition chosen was $M=6$ at 80,000-ft alt, with $M=4.5$ downstream of the vehicle bow shock and the equivalence ratio $\emptyset = 1.0$.

Figure 5 presents the inlet compression ramp flowfield streamlines. The ram consists of three 7° incremental deflec-

Table 1 Composition in mole fractions ($P=3$ atm, $T=333°K, \emptyset=1.0$)

Species	This program	General-purpose program [10]
N_2	0.56694	0.56684
H_2O	0.16394	0.16377
H_2	0.08216	0.08219
O_2	0.020880	0.02091
OH	0.05547	0.05551
H	0.06536	0.06540
O	0.02624	0.02627
NO	0.01901	0.01902

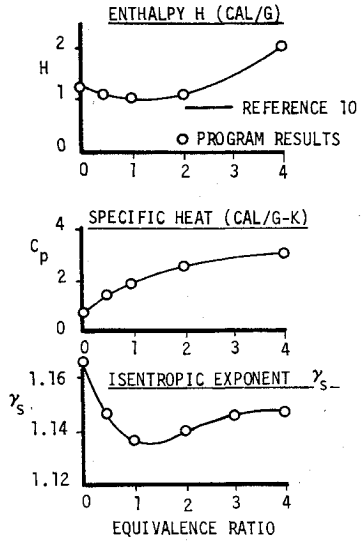

Fig. 3 Thermodynamic properties comparison ($P=3$ atm, $T=3333°K$, $\emptyset=1.0$).

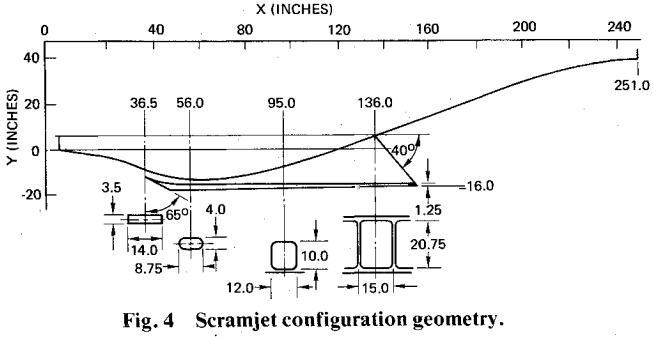

Fig. 4 Scramjet configuration geometry.

tions producing three weak shocks. This case provides a test of the program capability in the presence of multiple shocks. The computation grid consisted of 21 points. A comparison of the computed (real gas) and exact (ideal gas) solutions for the transverse pressure distributions at stations including one, two, and three shocks is shown in Fig. 6.

It is seen that in the case of the single and double shock the pressure ratios across the shock are predicted very well. However, as expected, the shocks are not defined sharply but are spread over several grid points. Because of the convergence of the three shocks, the shocks are smeared out completely at $x=28.7$, since only three to four grid points fall between them.

Figure 7 presents the inlet flowfield streamlines. The compression ramp flow properties were mass-averaged over the inlet height to obtain the start line data for the inlet. The inlet wall profile was approximated by a quadratic. Since the flow is assumed uniform and parallel to the inlet axis, a weak shock originated at the lip. The shock location can be inferred readily from the streamlines (Fig. 7) and tranverse pressure variations (Fig. 8). The interesting features of Fig. 8 are the

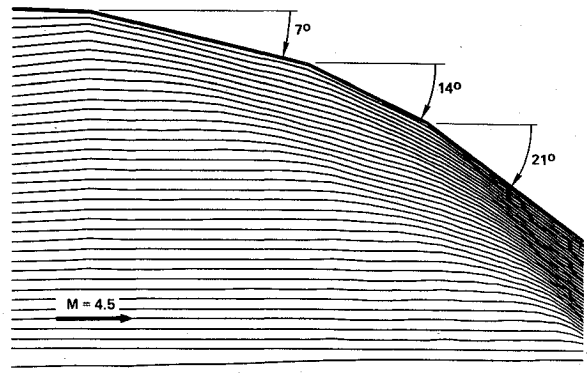

Fig. 5 Compression ramp flowfield.

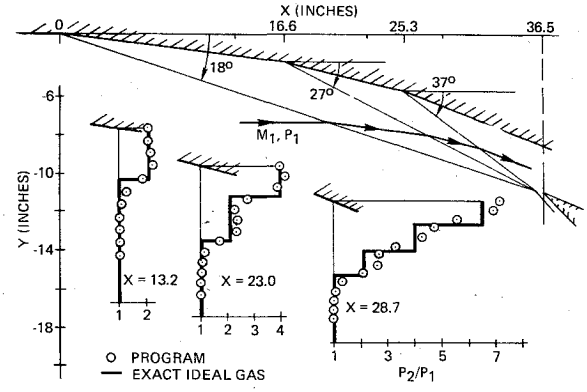

Fig. 6 Compression ramp flowfield transverse pressure variations.

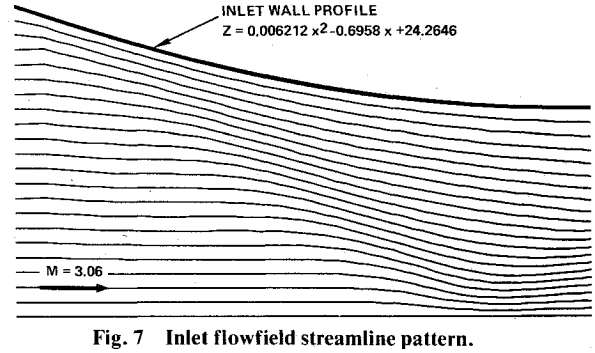

Fig. 7 Inlet flowfield streamline pattern.

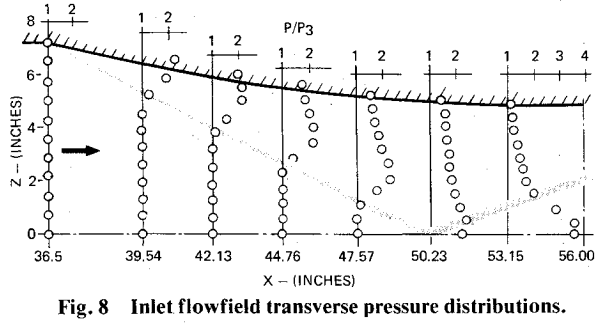

Fig. 8 Inlet flowfield transverse pressure distributions.

reflection of the lip shock and the inversion of the transverse pressure distribution as we proceed down the inlet.

The flowfield resulting from the interaction of the underexpanded scramjet exhaust, the vehicle afterbody, and the external stream is presented in Figs. 9-11, which show the streamlines, the afterbody surface and slip plane pressure variations, respectively. The effect of afterbody curvature ($X<196$) on the surface pressure is illustrated clearly in Fig. 10. An abrupt change in the surface pressure gradients is ap-

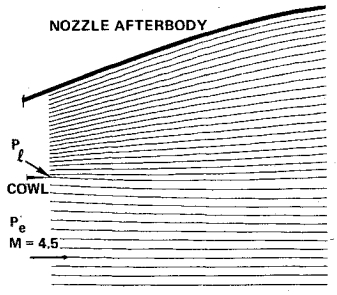

Fig. 9 Underexpanded exhaust/external stream interaction streamlines ($P_\ell/P_e = 2.25$).

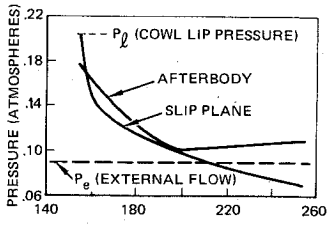

Fig. 10 Afterbody surface and slip plane pressures, underexpanded exhaust ($P_\ell/P_e = 2.25$).

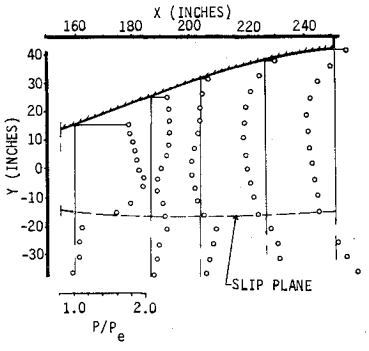

Fig. 11 Exhaust and external flow interaction transverse pressures, underexpanded exhaust ($P_\ell/P_e = 2.25$).

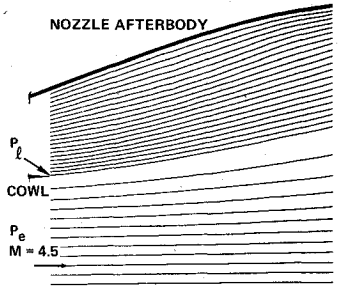

Fig. 12 Overexpanded exhaust/external stream interaction streamlines

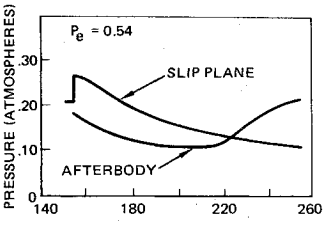

Fig. 13 Afterbody surface and slip plane pressures, overexpanded exhaust ($P_\ell/P_e = 0.375$).

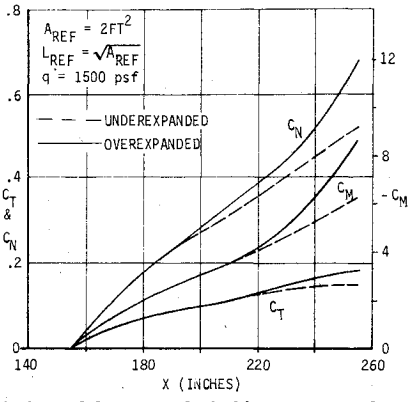

Fig. 14 Variation of forces and pitching moment due to afterbody surface pressure.

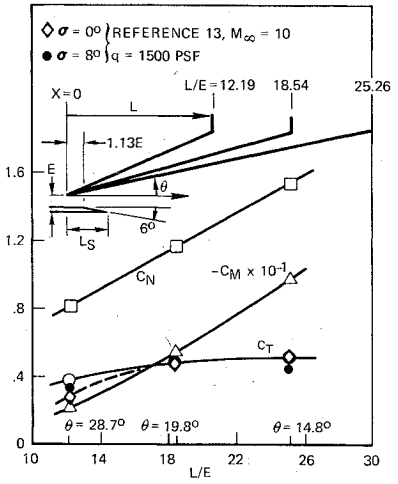

Fig. 15 Effect of afterbody length on scramjet performance ($\sigma = 8°$).

parent at station 196, followed by a gradual pressure rise, whereas, at the slip plane, the pressure continues to decrease below the external flow value. The transverse pressure distributions of Fig. 11 illustrate the complicated flowfield (not evident in the streamline plot of Fig. 9) resulting from the interaction of the underexpanded exhaust, the afterbody, and the external stream.

In order to illustrate and compare the effect of overexpanded nozzle flow, the external flow pressure was increased arbitrarily by a factor of 6. The resulting flowfield streamline plot and longitudinal pressure variations are presented in Figs. 12 and 13, respectively. Comparison of Figs. 10 and 13 shows that the afterbody surface pressures are practically identical up to approximately station 215. Beyond this station, the overexpanded case shows a sharp pressure rise due to the compression waves originating at the slip plane reaching the afterbody surface. The presence of the internal shock originating at the cowl lip is illustrated clearly by the sharp pressure rise at the slip plane at station 155 (Fig. 13). A comparison of the forces and moments acting on the afterbody is shown in Fig. 14, where it is seen that the overexpanded additional thrust is obtained at the expense of a large pitching moment, which could result in substantial trim-drag penalty.

The results of a parametric nozzle afterbody geometry analysis are presented in Figs. 15 and 16. The objective of this analysis was to compare the nozzle force characteristic trends obtained by means of the present program with those of Ref. 12 obtained by means of the three-dimensional reference plane characteristic computer program. Since most of the results presented in Ref. 12 include total vehicle aerodynamics, whereas the present analysis is restricted to the isolated nozzle characteristics, only the trends are compared.

The effect of varying the nozzle afterbody length and slope on the engine force characteristics is shown in Fig. 15; the corresponding thrust coefficient values from Ref. 12 are shown for comparison. The reference area for this analysis was chosen such that the C_T data for the case of $L/E = 18.8$ (nozzle/afterbody length to nozzle inlet height ratio) matched those of Ref. 12. It is seen that C_T increases with increasing nozzle length accompanied by a considerable increase in pitching moment. The slight difference between the C_T trends of the present analysis and those of Ref. 12 most probably is due to difference in flight Mach number and the σ angle bet-

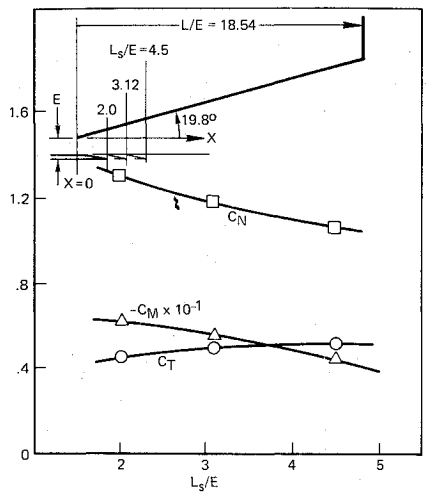

Fig. 16 Effect of cowl length on scramjet performance.

ween the engine and flight axes which is independent on vehicle geometry.

The effect of cowl length on the nozzle force characteristics is shown in Fig. 16. The trends are again in agreement with those presented in Ref. 12; i.e., C_T increases and C_M decreases with increasing L_s/E as a result of the increased expansion ratio at the nozzle exit plane and the reduction of the afterbody surface pressure forces.

IV. Concluding Remarks

The results of the two-dimensional flow analyses presented illustrate the complexities of the flowfields associated with scramjets. Also, it is seen that the overall integrated scramjet-vehicle performance and stability can be influenced to a large degree by the design of the nozzle afterbody geometry, that is, the appropriate choice of nozzle/afterbody length, nozzle slope (expansion ratio), and the contour of the afterbody.

In summary, it is believed that the program described herein provides a rapid and accurate means of performing scramjet flowfield and performance analyses for preliminary design and parametric studies. It is felt that the program deficiencies resulting from neglect of three-dimensional flow effects are more than compensated for by the programs speed, ease of input data handling, and program flexibility provided by the integral thermodynamic properties subprogram. This program, in conjunction with the available, more complex, three-dimensional scramjet flowfield programs, should prove to be a valuable preliminary design tool.

References

[1] Henry, J.R. and McLellan C.H., "Air-Breathing Launch Vehicles for Earth Orbit Shuttle-New Technology and Development Approach," *Journal of Aircraft*, Vol. 8, May 1971, pp. 381-387.

[2] Ferri, A., "Review of Scramjet Propulsion Technology," *Journal of Aircraft*, Vol. 5, Jan.-Feb. 1968, pp. 3-10.

[3] Dugger, G.L., "Comparison of Hypersonic Ramjet Engines with Subsonic and Supersonic Combustion," *AIAA Selected Reprints*, Vol. VI, Ramjets, June 1969.

[4] Johnston, P.J., Cubbage, J.M., and Weidner, J.P., "Studies of Engine-Airframe Integration on Hypersonic Aircraft," *Journal of Aircraft*, Vol. 8, July 1971, pp. 495-501.

[5] Del Guidice, P., "Three Dimensional Nozzle Flow Fields by a Reference Plane Technique-Including the Effects of Equilibrium Hydrogen-Air Chemistry, Ph.D. Thesis, June 1972, New York Univ., New York City.

[6] Dash, S., Del Guidice, P., and Kalben, P., "Analysis and Design of Three-Dimensional Supersonic Nozzles," CR-132350, Vols. I and II, NASA 1972.

[7] Sadunas, J.A., "Two-Dimensional Real Gas Scramjet Flow Fields," Rockwell International, Space Division, Downey, Calif., Rept. SD74-SA-0131, Oct. 1974.

[8] Kutler, P., Warring, R.F., and Lomax, H., "Computation of Space Shuttle Flow Fields Using Noncentered Finite-Difference Schemes," *AIAA Journal*, Vol. 11, Feb. 1973, pp. 196-204.

[9] Kutler, P. and Lomax, H., "A Systematic Development of the Hypersonic Flow Fields Over and Behind Wings and Wing Body Configurations Using a Shock Capturing Finite-Difference Approach," *Journal of Spacecraft and Rockets*, Vol. 8, Dec. 1971, pp. 1175-1181; also AIAA Paper 71-99, N.Y.C., N.Y. 1971.

[10] Gordon, S. and McBride, B.J., "Computer Program for Calculation of Complex Chemical Equilibrium Compositions, Rocket Performance, Incident and Reflected Shocks and Chapman-Jouguet Detonation," NASA SP-273, 1971.

[11] Van Camp, V.V. and Williams, E.T., "Hypersonic Research Airplane Propulsion for Boost and Test," *Journal of Aircraft*, Vol. 12, July 1975, pp. 611-616; also AIAA Paper 74-990, Los Angeles, Calif., 1974.

[12] Edwards, C.L.W., Small, W.L., Weidner, J.P., and Johsnton, P.J., "Studies of Scramjet/Airframe Integration Techniques for Hypersonic Aircraft," AIAA Paper 75-58, San Diego, Calif., Jan. 1975.